Research Article | Vol. 27, No. 24 / 25 November 2019 / Optics Express 35129

Optics EXPRESS

Tuning silicon-rich nitride microring resonances with graphene capacitors for high-performance computing applications

JOAQUIN FANECA,[1,2,3,*] BENJAMIN T. HOGAN,[1,2] IAGO R. DIEZ,[1,2] FREDERIC Y. GARDES,[3] AND ANNA BALDYCHEVA[1,2]

[1] University of Exeter, College of Engineering Mathematics and Physical Sciences, Exeter, EX4 4QF, UK
[2] EPSRC Centre for Doctoral Training in Electromagnetic Metamaterials, University of Exeter, EX4 4QL, UK
[3] Optoelectronics Research Centre, Building 53, University of Southampton, SO17 1BJ, UK
[*] jkin03@gmail.com

Abstract: We demonstrate the potential of a graphene capacitor structure on silicon-rich nitride micro-ring resonators for multitasking operations within high performance computing. Capacitor structures formed by two graphene sheets separated by a 10 nm insulating silicon nitride layer are considered. Hybrid integrated photonic structures are then designed to exploit the electro-absorptive operation of the graphene capacitor to tuneably control the transmission and attenuation of different wavelengths of light. By tuning the capacitor length, a shift in the resonant wavelength is produced giving rise to a broadband multilevel photonic volatile memory. The advantages of using silicon-rich nitride as the waveguiding material in place of the more conventional silicon nitride (Si_3N_4) are shown, with a doubling of the device's operational bandwidth from 31.2 to 62.41 GHz achieved while also allowing a smaller device footprint. A systematic evaluation of the device's performance and energy consumption is presented. A difference in the extinction ratio between the ON and OFF states of 16.5 dB and energy consumptions of <0.3 pJ/bit are obtained. Finally, it has been demonstrated that increasing the permittivity of the insulator layer in the capacitor structure, the energy consumption per bit can be reduced even further. Overall, the resonance tuning enabled by the novel graphene capacitor makes it a key component for future multilevel photonic memories and optical routing in high performance computing.

1. Introduction

Photonic integrated circuits (PICs) overcome the major drawbacks that electronics faces today, particularly in terms of the limited transmission speed and high power consumption, by using light to process, transmit and store information [1]. PICs based on silicon-rich nitride (SRN) waveguide platforms demonstrate enhanced operation [2] due to their: tuneable non-linearity and refractive index; low temperature sensitivity; low optical losses; stronger mode confinement than Si_3N_4 while maintaining a better interaction with the deposited materials than silicon-on-insulator (SOI); and most importantly, broadband transparency spanning infrared and visible wavelength ranges [3,4]. Currently, the library of developed and tested individual photonics components for integration into PIC systems is extensive. However, one of the main challenges inherent to standard photonics components is the high cost of the SOI material platform, and associated high-cost of production, due to the complex multi-stage fabrication processes involved [5]. Implementation of reconfigurable materials is the most promising solution, since the complexity of designs for actively tuneable devices can be simplified. Beyond the well-established reconfigurable materials,

#378472 https://doi.org/10.1364/OE.27.035129
Journal © 2019 Received 23 Sep 2019; revised 29 Oct 2019; accepted 1 Nov 2019; published 15 Nov 2019

Optics EXPRESS

such as phase change materials (PCMs) [6], liquid crystals [7] and p-n junctions technology [8–10], new technologies are emerging, such as: hyperbolic metamaterials based optical modulators [11], and nano-opto-mechanical effects in integrated waveguides [12]. Graphene and graphene-related materials [13] are truly outstanding candidates for application in reconfigurable PICs, with the potential to facilitate endless opportunities for construction of reconfigurable integrated photonic components such as modulators [14–17], switchers [18], and photodetectors [19]. Graphene is attracting significant interest from the photonics community due to its unique combination of thermal, electronic, and optical characteristics [20]. The linear dispersion found around the Dirac points in graphene's band structure leads to the universal optical conductance of the interband transition [21,22]. Single-layer graphene demonstrates broad conductive transparency - it absorbs only 2.3% of normally incident light within the infrared-to-visible spectral range. The density of states of carriers near the Dirac points is low, and as a consequence, graphene's Fermi energy can be tuned significantly with relatively low electrical energy required [23]. This Fermi level tuning changes the refractive index (RI) of the graphene. Thus combining graphene with integrated silicon waveguides opens great possibilities for the design of tuneable components in PICs. Herein, we propose a graphene capacitor as the key component for future volatile multilevel photonic memories (VMPM). Volatile memories find their main applications in general-purpose random-access memories, and in data security systems for the protection of sensitive information [24]. To date, integrated photonic volatile memories have been demonstrated as solutions for optical logic processing [25,26], ensuring data security [27], quantum computing [28], and deep learning. We describe the first graphene-enabled VMPM concept based on a multiplexed design of SRN micro-ring resonators structures on chip Fig. 1. The proposed SRN platform allows high density memory integration through multilevel stacking of SRN layers achieved via the low temperature fabrication process recently developed by Bucio *et al.* [29]. First, we introduce the concept and designs of electrically-driven graphene capacitor structures integrated

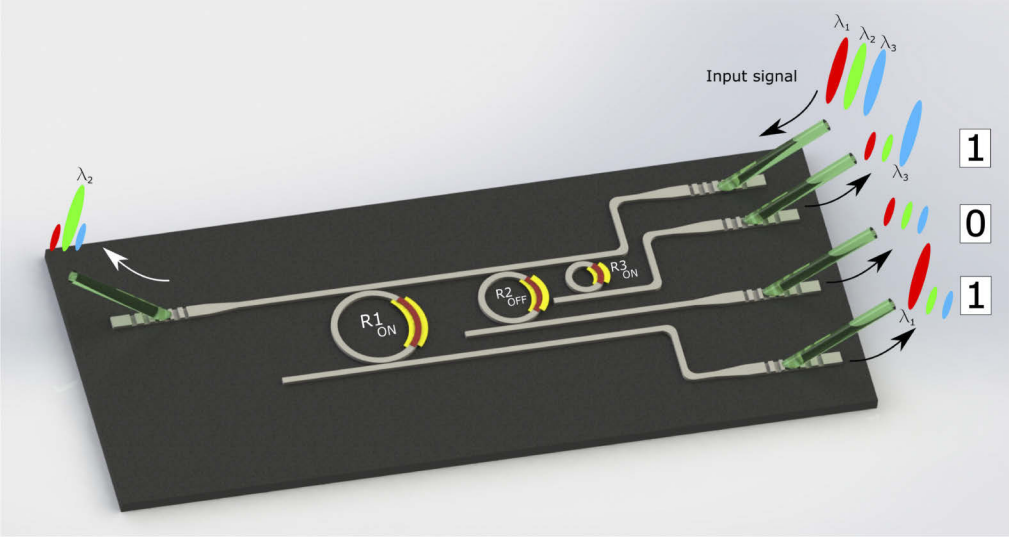

Fig. 1. Schematic of the integrated parallel volatile photonic memory based on a multiplexed system of hybrid graphene capacitor-SRN microring circuits. The photonic circuit consist of three microrings of radii R_1, R_2, R_3 with integrated graphene capacitor sections (graphene-red; electrical contacts- yellow). The schematic depicts coding for the binary number "101" where transmission of different wavelengths is tuned by switching the graphene capacitors 'ON' or 'OFF' on different rings.

Optics EXPRESS

with SRN photonic waveguides and microring structures. This is followed by a systematic study of the operational performance depending on the geometrical parameters of the designs. We then introduce the concept and designs of triple microring systems and assess the operational characteristics in the context of VMPM applications.

2. Design and modelling of a reconfigurable graphene capacitor based on electric field effect in SRN micro-ring resonators

2.1. Graphene capacitor optical modelling

The device we consider (shown in Fig. 1) consists of a SRN waveguide structure partially covered by a graphene capacitor structure. The graphene capacitor consists of a thin layer of (Si_3N_4) insulating material sandwiched between two layers of graphene electrodes [30] (shown in Fig. 2(a)). To accurately assess the operation of electrically-tuneable hybrid waveguides based on graphene capacitors (HWGCs) within the optical communications wavelength range, the optical properties of graphene must first be defined. One of the most important functional characteristics of graphene is its gate-variable optical conductivity [31]. Graphene's conductivity can be tuned by the application of a voltage to a graphene capacitor structure. Applying the voltage changes the carrier density of graphene and, consequently, the Fermi level. The dependence of graphene's optical conductivity on inter- and intra-band transitions has previously been analytically derived at 0K and at 300K [32]. The complex optical conductivity $\sigma(\omega, \mu, \Gamma, T)$ depends on the temperature, T, the angular frequency, ω, the Fermi level, μ, and the charge particle scattering rate, $\Gamma = \tau^{-1}$, where τ is the relaxation time, and can be described as [33] :

$$\sigma_t(\omega, \mu, \Gamma, T) = \sigma_{intra} + \sigma'_{inter} + \sigma''_{inter} \tag{1}$$

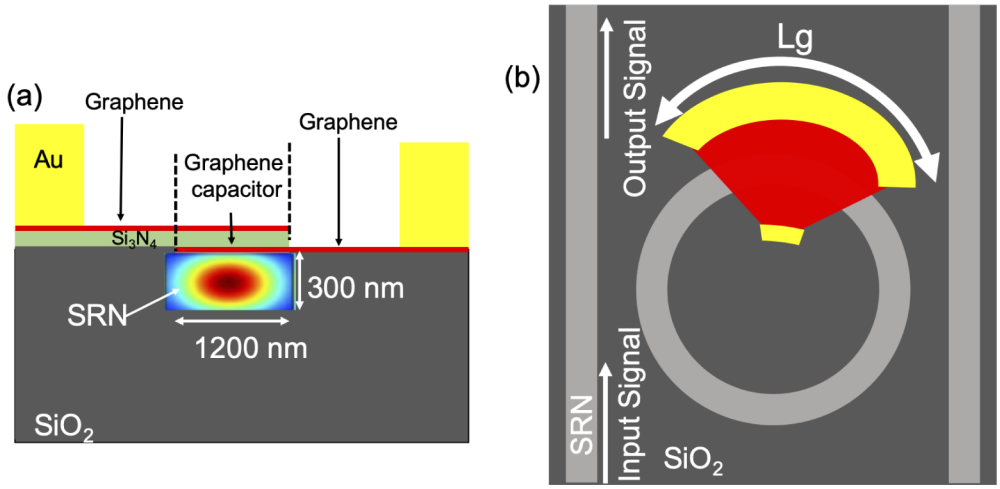

Fig. 2. (a) Schematic cross-section of the HWGC structure - a SRN ridge waveguide with a graphene-(Si_3N_4) capacitor on top. (b) Top view of an embedded micro-ring resonator partially covered by a graphene capacitor incorporating golden contacts for the application of a voltage to the device.

The intraband conductivity σ_{intra} follows Drude's model:

$$\sigma_{intra} = \frac{4\sigma_0\mu}{\pi(\hbar\tau_1^{-1} - j\hbar\omega)}, \tag{2}$$

where $\sigma_0 = \pi e^2/2h$ is the universal optical conductance and τ_1^{-1} is the relaxation rate associated with intraband transitions.

Optics EXPRESS

The interband contribution can be described as:

$$\sigma_{inter}^{'} = \sigma_0 \left(1 + \frac{1}{\pi} tan^{-1}\left(\frac{\hbar\omega - 2\mu}{\hbar\tau_2^{-1}}\right) - \frac{1}{\pi} tan^{-1}\left(\frac{\hbar\omega + 2\mu}{\hbar\tau_2^{-1}}\right)\right) \tag{3}$$

and

$$\sigma_{inter}^{''} = -\frac{\sigma_0}{2\pi} ln\left(\frac{(2\mu + \hbar\omega)^2 + \hbar^2\tau_2^{-2}}{(2\mu - \hbar\omega)^2 + \hbar^2\tau_2^{-2}}\right), \tag{4}$$

where τ_2^{-1} is the relaxation rate associated with inter-band transitions. The complex dielectric function, $\varepsilon(\mu)$, can be obtained from the complex optical conductivity through the relationship:

$$\varepsilon(\mu) = 1 + \frac{j\sigma(\mu)}{\omega\varepsilon_0\delta}, \tag{5}$$

where δ is the graphene thickness layer (0.7 nm or 0.4 nm depending on the fabrication accuracy [34]), and ε_0 is the vacuum permittivity. The Fermi level is directly linked to the surface charge density, n_s, by the following relation:

$$\mu = \frac{h\nu_F}{2\pi}\sqrt{\pi|n_s|}, \tag{6}$$

where $h \simeq 6.62 \cdot 10^{-34} m^2 \cdot kg \cdot s^{-1}$ is Planck's constant and $\nu_F \simeq 9.5 \cdot 10^7 cm \cdot s^{-1}$ is the Fermi velocity. Graphene's charge surface density, and consequently the Fermi level, can be actively tuned by application of voltage to the capacitor structure. The applied voltage, V, required to adjust the Fermi level to a value μ can be described as:

$$|V| = \frac{en_s}{C} + 2\frac{\mu}{e}, \tag{7}$$

$$|V| = \frac{e}{\pi(h\nu_F)^2} \cdot \frac{\mu^2}{C} + 2\frac{|\mu|}{e}, \tag{8}$$

where e is the charge on an electron, and $C = \frac{\varepsilon_0\varepsilon_{ins}}{t_{ins}}$ is the capacitance per unit area, determined by insulating layer's relative permittivity, ε_{ins}, and thickness, t_{ins}.

The complex dielectric function, or consequently the refractive index, $n^2(\mu) = \varepsilon(\mu)$, determines the mode supported by the SRN waveguide structure. To facilitate interaction between a propagating mode in the waveguide and the graphene capacitor on top, the Fermi level should be tuned to a position between the valence and conduction bands. The main principle of operation for the device is the same as that for graphene optical modulators [35]; energy is transferred from photons in the propagating mode to the electrons in the graphene electrodes (photons are "absorbed"). If the Fermi level is situated above the conduction band or below the valence band, no photon absorption occurs, as either the bands are both filled (and there is nowhere for electrons to go when gaining energy) or both empty (and there no electrons to gain energy) respectively [19].

2.2. Mode analysis

The device characteristics were simulated for a wavelength of 1550 nm and a SRN (n = 2.54) ridge waveguide cross-sectional area of 1200 x 300 nm was selected to give a single-mode integrated waveguide. By using the commercial software COMSOL Multiphysics, the graphene capacitor structure on top of a ridge waveguide was then analysed. We determined the profile of the propagating mode within the SRN waveguide and how this mode is affected by the graphene capacitor at different voltages. This change has been quantified in terms of change of the effective

Optics EXPRESS

refractive index $n_{eff} = n^c_{eff} + jk^c_{eff}$ experienced by the mode. We consider a graphene capacitor consisting of a $t_{ins} = 10$ nm of Si_3N_4, ($\varepsilon_{ins} = 4$) acting as insulator between two graphene layers. To achieve electro-absorption operation in the graphene capacitor, the Fermi level (μ) should reach the breakdown value of 0.5 eV (see Fig. 3). Through Eq. 6 a graphene charge density $n_s = 2 \cdot 10^{13} cm^2$ is needed in order to shift the Fermi level to $\mu = 0.5$ eV. This corresponds to an electric field across the capacitor insulator of:

$$E_{0.5eV} = \frac{qn_s}{\varepsilon_{ins}\varepsilon_0} \approx \frac{3.6 \cdot 10^7}{\varepsilon_{ins}} \left[\frac{V}{cm}\right] \tag{9}$$

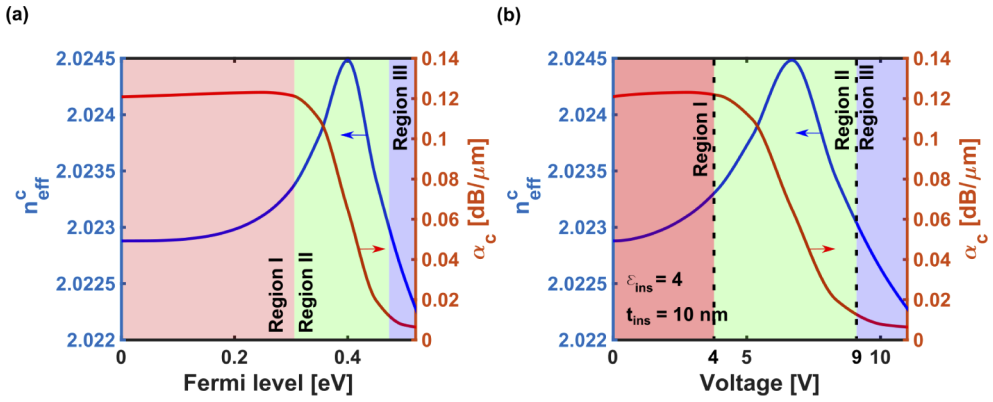

Fig. 3. The effective refractive index of the mode propagating in the hybrid structure made of a graphene capacitor on top of a 1.2 x 0.3 μm SRN (n=2.54) ridge waveguide, plotted against (a) the graphene's Fermi level and (b) the voltage applied to the capacitor. The graphene capacitor is made of a layer of 10 nm of (Si_3N_4) acting as the insulator between two graphene sheets. The real part of the n_{eff}, n^c_{eff}, is represented by the blue line (left y-axis) and the imaginary part (k^c_{eff}), expressed in terms of the loss coefficient, is represented by the red line (right y-axis).

where ε_{ins} is the relative dielectric constant of the insulator. Equation 9 determines which insulators allow device operation without reaching the dielectric breakdown limit. For example, silicon dioxide (SiO_2, $\varepsilon_{ins} = 2.9$ [36]), requires $E_{0.5eV} = 9.3 \cdot 10^6$V/cm which is close to the breakdown fields of thermal SiO_2 thin films (on the order of 10^7V/cm [36]). Similarly, alumina (Al_2O_3 with $\varepsilon_{ins} = 9$ [37]) requires $E_{0.5eV} = 4 \cdot 10^6$V/cm, which is again very close to the reported breakdown fields of Al_2O_3 [37]. However, silicon nitride (Si_3N_4, $\varepsilon_{ins} = 4$ [38]) represents a suitable alternative with $E_{0.5eV} = 5 \cdot 10^6$ V/cm to be compared to a breakdown field on the order of 10^7V/cm [39].

From the mode profiles, we calculated the real and imaginary part of the mode's n_{eff}, i.e. $n^c_{eff}(\mu)$ and $k^c_{eff}(\mu)$ respectively, for a range of Fermi levels between 0 and 0.55 eV. $k^c_{eff}(\mu)$ is equivalent to the loss coefficient $\alpha_c[dB/\mu m] = 4.34(4\pi k^c_{eff})/\lambda$. We focused our attention on the TE mode because light with this polarization interacts with the in-plane dielectric permittivity of graphene sheets, as the E-field is parallel to the graphene plane.

Figure 3(a) shows the effect on the mode's n_{eff} as the Fermi level is varied. The maximum value for the voltage is limited by the breakdown electrical field strength of the silicon nitride insulator between the two graphene layers which has a value of 11MV/cm [39], i.e. 11V for the thickness of 10 nm as used here. Three different regimes can be defined in terms of the loss coefficient, α_c. In Region I: for $\mu < 0.4$ eV graphene exhibits a high loss state. In Region II: for values around $\mu \sim 0.4$ eV the transition from high to low loss occurs. In Region III: for $\mu > 0.4$

Optics EXPRESS

eV, graphene exhibits a low loss state and acts as a quasi-transparent material. Equation 8 allows us to directly exchange the Fermi level values for voltage values, and thus, plot the mode's n_{eff} in terms of the voltage applied to the graphene capacitor as in Fig. 3(b). In terms of the voltage, we have: Region I: 0-4 V, OFF state, high loss; Region II: 4-9 V, transition state; Region III V>9V, ON state, low loss.

2.3. Ring resonator

Among various silicon photonic devices structures for multichannel applications, silicon microring resonators possess many advantages such as wavelength agility, high quality factors ($10^5 - 10^6$), high sensitivity and compact footprint. Silicon micro-ring resonators have been employed as core building blocks for optical multiplexers and demultiplexers [40–42]. The light in a micro-ring resonator is coupled from the waveguide by the evanescent field of the mode and is partially confined along the cavity sidewall by total internal reflection (TIR). The cavity field phase matches with itself upon each round trip for specific wavelengths, giving rise to an optical resonance. The resonance phase-matching condition is given as follows:

$$n_{eff} L = m\lambda_m \tag{10}$$

where n_{eff} is the effective refractive index of the micro-ring resonator waveguide, L is the cavity round-trip length, λ_m is the m_{th} order resonance wavelength in free space, and m is the integer number of wavelengths along an optical round-trip length. In the case of a micro-ring with radius R, L is given by $2\pi R$. By positioning the graphene capacitor on top of the ring resonator, as shown in Fig. 2(b), the n_{eff} of the microring can then be modified by applying a voltage across the graphene capacitor (see Fig. 3(b)). The change in n_{eff} allows the reconfigurability of the ring resonator resonances [43]. A Transfer Matrix Method (TMM) [44] was used to model the performance of reconfigurable micro-ring resonators with a gap between the waveguide and the rings of 300 nm.

3. Results and discussion

3.1. Passive tuning

In addition to the active tuning already discussed, a passive tuneability of the devices is inherent in the fabrication process. By choosing the length of the graphene capacitor structure (L_g), the effective refractive index of the ring can be further tuned. The choice of this parameter is crucial because it cannot be modified after fabrication, contrary to the actively tuneable voltage mechanism. By increasing the length of the capacitor, the degree of interaction between the mode and the capacitor structure increases. This causes a shift in the resonance of the ring resonator structures as shown in Fig. 4(a). In terms of the spectral response, increasing the length of the graphene capacitor gives rise to a red shift of the ring resonator resonance. In Fig. 4(b) the resonance shift produced by the different capacitor lengths with the corresponding extinction ratio achieved for given dimensions of the capacitor is shown. For example, a 6.4 nm shift can be achieved using a graphene capacitor that covers 25% of the ring resonator. Different voltages V_{ON} and V_{OFF} are used to tune the extinction ratio (ER) of each of the graphene capacitor lengths individually. Figure 4(b) also shows how the difference in the extinction ratio between the ON and OFF states decreases when the length of the capacitor increases for the same ring resonator radius ($R = 65\mu$m).

3.2. Graphene enable high performance computing

Exploiting the electro-absorption effect of the graphene capacitor modulator (Region II: 4V - 9V) to tune the imaginary part of the n_{eff} of graphene paves the way for photonic volatile multi-level memory and optical routing. The proposed device is based on SRN micro-ring

Optics EXPRESS

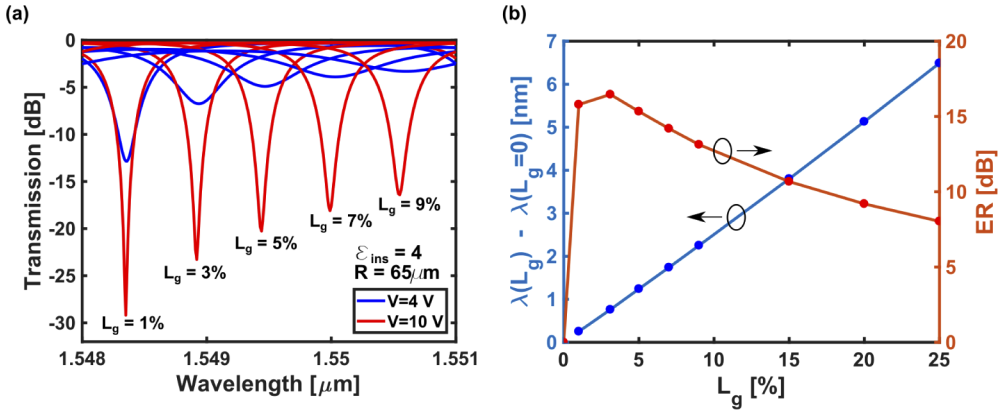

Fig. 4. (a) Resonant wavelength as a function of the length of graphene capacitor for a fixed ring resonator radius ($R = 65\mu$m). (b) Resonant wavelength shift produced by the graphene capacitor for different lengths (blue) and extinction ratio difference achieved for different graphene capacitor length (red).

resonators placed as add-drop filters with a single input waveguide and N output waveguides, with N being, the number of micro-ring resonators. An example with $N = 3$ is depicted in Fig. 1. The operation of the device is based on controlling the transmission for each of the channels by tuning the voltage of the individual HWGC structures. Here we consider a device consisting of three ring resonators with ring radii of R_1=70 μm, R_2=65 μm and R_3=60 μm. Different resonant frequencies ($\lambda_1 = 1.55497\ \mu m\ \lambda_2 = 1.55475\ \mu m$ and $\lambda_3 = 1.55451\ \mu m$) are resonantly coupled to each ring respectively. The voltage-dependent transmission measured through the input waveguide is plotted in Fig. 5(a) for the three ring resonators. A state of high transmission through the input waveguide corresponds to a low transmission from the output waveguide (OFF state). We can define this OFF state as a 0-bit. A state of low transmission through the input waveguide corresponds to a high transmission from the output waveguide (ON state). We can define this ON state as an 1-bit. Therefore, a 0 or 1 in the output bus waveguide of each channel will be measured depending on the voltage applied to the corresponding HWGC. Three ring resonators are used with two possible states each; hence 2^3 possible configurations can be achieved. The 2^3 possible codifications are shown in Fig. 5(b). The number of combinations can be increased by increasing the number of ring resonators. This presents a trade-off between the number of combinations and the footprint of the device. SOI waveguides can increase the number of rings in a smaller footprint (higher density) of the proposed device, but the interaction between the mode and the graphene capacitor will be smaller due to the strong confinement of the modes. SRN can allow a greater interaction with the graphene capacitor than silicon and at the same time can confines the mode more strongly than (Si_3N_4). Using SRN, the distance (d_s), as shown in Fig. 6, can be reduced compared with Si_3N_4 allowing faster devices and smaller footprint while maintaining the same ER.

3.3. Electrical simulations

In order to calculate the speed of the device and the time response, we define an equivalent RC circuit as shown in Fig. 6(a). The time response of the RC circuit can be calculated using $V(t) = V_0 e^{-t/\tau}$ where $\tau = RC$ and the speed of the device can be calculated using the response bandwidth, which is determined by:

$$Bdw = \frac{1}{2\pi[2(R_c + R_s)] \cdot C} \tag{11}$$

Optics EXPRESS

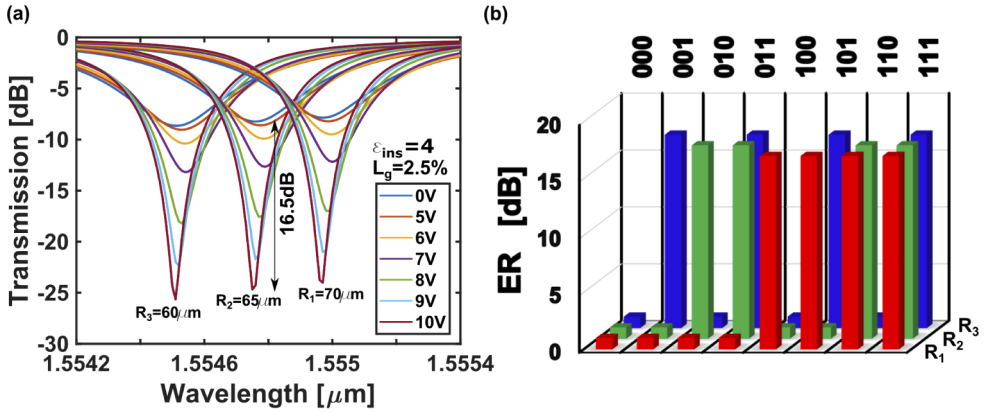

Fig. 5. (a) Transmission at the input waveguide for three different ring resonators with radii R_1=70 μm, R_2=65 μm and R_3=60 μm and different voltages applied individually to each of the rings. (b) Binary coding combinations obtained by individually tuning each ring resonator graphene capacitor. The extinction ratio difference (ER) between the ON and OFF states at the output waveguides for each of the individual ring resonators (R_1, R_2 and R_3) allows one to code 2^3 combinations.

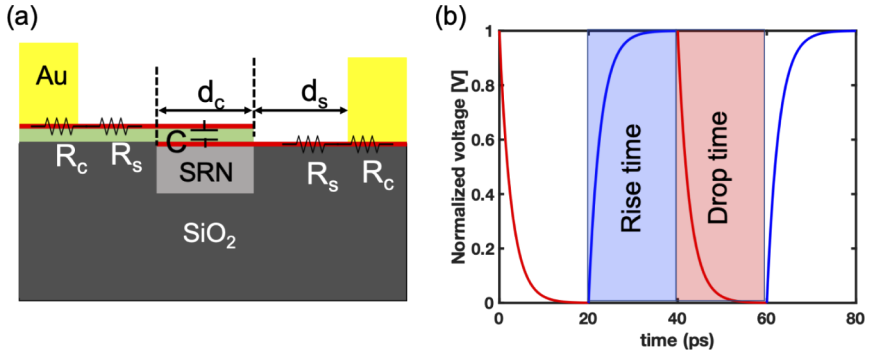

Fig. 6. (a) HWGC cross-section showing the defined equivalent circuit of the graphene capacitor and contacts where R_c, R_s are the contact and the sheet resistance respectively and C is the capacitance. d_c is the graphene capacitor width and d_s is the distance between the contacts and the waveguide. (b) Time response of the HWGC.

where R_c and R_s are the contact and sheet resistances of graphene respectively, and C is the capacitance of the device. The contact resistance of graphene emerges from the Fermi level mismatch between the graphene and the metallic electrodes. This parameter depends on the quality of the graphene and the metal selected for the electrode [45]. Experimental results have previously shown values of the contact resistivity (ρ_c) in the range of 100 to 1000 $\Omega\mu m$ [46,47]. The total contact resistance of graphene is calculated as $R_c = \rho_c/L_g$. The graphene's sheet resistance, is usually defined by the resistance per square, R_{SQ}. The values of R_{SQ} for graphene are typically between 100 and 500 Ω/sq [48–50], in all of our calculations, we assume a conservative value of 500 Ω/sq. To obtain the total sheet resistance of graphene, we need to consider the contribution of all the squares constituting the device. The total sheet resistance can be expressed as $R_s = R_{SQ} \cdot \frac{d_s}{L_g}$. The width of the graphene capacitor is selected to be d_c=1.2 μm entirely covering the waveguide as shown in Fig. 6. Using a (Si_3N_4) waveguide, the distance between the gold contacts is selected to be 1 μm to ensure that the metal does not contribute

Optics EXPRESS

to the losses. A bandwidth response of 12.5 GHz has been calculated in this case. Using SRN as the waveguide material instead of Si_3N_4, the contacts can be closer to the waveguide (400 nm) without affecting the mode propagation (see Fig. 7(a)), reducing by 600 nm the distance between the graphene capacitor and the golden contact compared with Si_3N_4. Consequently, R_s is reduced and the calculated device bandwidth increases to 15.6 GHz. For the best case scenario of contact resistance ($\rho_C = 100\ \Omega\mu m$) maintaining a conservative value in the sheet resistance ($R_{SQ} = 500\ \Omega/sq$), the bandwidth will increase up to 31.2 GHz and 62.41 GHz for Si_3N_4 and SRN respectively (see Fig. 7(b)). Examining Eq. 11 one can observe that when the capacitance and resistances are multiplied, the length of the device L_g is cancelled out; therefore, the length of the device has no impact on the response bandwidth and only influences the insertion losses (IL). The IL per unit length of our graphene capacitor devices are 0.13 dB/μm and 0.01 dB/μm for the OFF and ON states respectively (shown in Fig. 3).

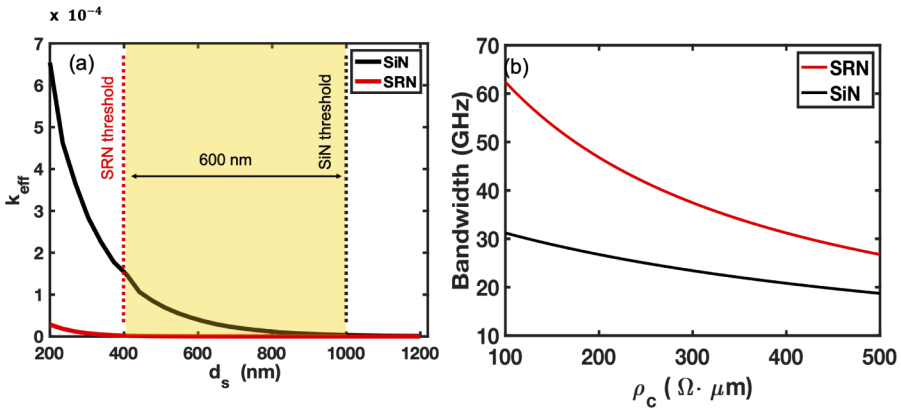

Fig. 7. (a) Parametric sweep study of the k_{eff} in the mode against the distance between the contact and the graphene capacitor (d_s) for values between 200-1200 nm for Si_3N_4 (black line) and for Silicon Rich Nitride (SRN) (red line) (b) Parametric sweep study of the contact resistance for Si_3N_4 platform (black line) and for SRN (red line). The ridge waveguide dimensions are 1200 nm width and 300 nm thick.

3.4. Energy consumption

The average energy consumption of the devices, expressed as energy per bit, is given by the formula:

$$E_b = \frac{1}{4}CV^2 = \frac{1}{4}\frac{\varepsilon_0\varepsilon_{ins}}{t_{ins}}L_g \cdot d_c \cdot [V_{ON} - V_{OFF}]^2 \tag{12}$$

In the proposed device, the graphene capacitor lengths for each ring resonator are $L_g^1 = 10.9956\ \mu$m, $L_g^2 = 10.2102\ \mu$m and $L_g^3 = 9.4248\ \mu$m. The energy consumptions per bit (E_b) for each ring resonator (R_1, R_2 and R_3) respectively are $E_{b1} = 0.2921$ pJ/bit, $E_{b2} = 0.2712$ pJ/bit and $E_{b3} = 0.2503$ pJ/bit, respectively. The energy per bit can be reduced by either: reducing the thickness of the insulator (but that will increase the capacitance and reduce the speed of the device); or increasing the permittivity of the graphene capacitor insulator, as indicated in Fig. 8(b). By increasing the permittivity the difference between the ON and OFF voltages is reduced. From Eq. 12 it can be seen that the voltage dependence is quadratic whereas the permittivity dependence is linear, giving the overall effect that E_b will be reduced. The relation between the energy consumption per bit of the device and the extinction ratio achieved for different graphene capacitor lengths is shown in Fig. 8(a). The behaviour of the threshold voltage for different insulator permittivities is shown in Fig. 8(b). Increasing the insulator permittivity, the

Optics EXPRESS

threshold voltage is reduced and paves the way to lower power consumption devices for future reconfigurable photonic integrated circuits in optical communications applications. The devices IL due to the graphene capacitor are around 1.3 dB in the OFF state and 0.1 dB in the ON-state.

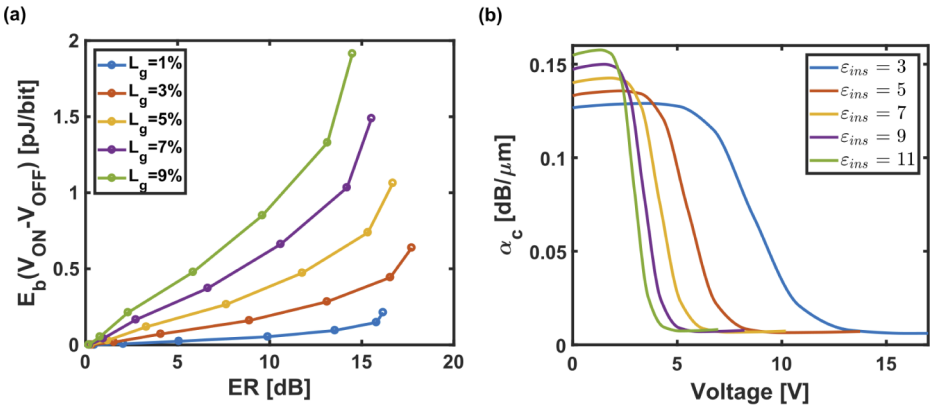

Fig. 8. (a) Plot of the energy per bit against the Extinction Ratio (*ER*) between the ON and OFF state achieved for different lengths of the graphene capacitor. For each curve, each circle marker corresponds to a different value of V_{ON} used for the ON-state, at 1V intervals; with the first marker representing 5V and the last one 11V. In all cases, the values used for the OFF-state is $V_{OFF} = 4V$. (b) The loss coefficient α_c of the guided mode along the HWGC structure against the operating voltage. Several curves are plotted for different values of the dielectric constant of the insulator between the plates of the capacitor, ε_{ins}.

4. Conclusions

We have shown the potential of a graphene capacitor structure on SRN micro-ring resonators for multitasking and HPC. The electro-absorption effect can be used to develop multilevel volatile memories for communications applications, optical routing and binary coding. By tuning the capacitor length, a shift in the resonant wavelength is produced giving rise to a broadband multilevel photonic volatile memory. An increase in the device speed has been shown to be achieved by using a silicon rich nitride (SRN) waveguide in place of Si_3N_4, due to the increased confinement of the propagating mode allowing a smaller device footprint. We demonstrated that it is possible to double the speed of the devices from 31.2 GHz up to 62.41 GHz in this way. A study of the relation between the device energy consumption, extinction ratio and capacitor length has been shown. Finally, it has been demonstrated that increasing the permittivity of the insulator layer in the capacitor structure, the energy consumption per bit can be reduced.

Funding

Engineering and Physical Sciences Research Council (EP/L015331/1, EP/L021129/1, EP/N013247/1, EP/N035569/1); Horizon 2020 Framework Programme (688516 COSMICC); Royal Society International Exchange Programme (2015/R3).

Acknowledgments

We acknowledge Titouan Le Paven for his contribution to some of the figures and developing part of the code to achieve the results.

Optics EXPRESS

Disclosures

The authors declare no conflicts of interest.

References

1. G. T. Reed, G. Mashanovich, F. Y. Gardes, and D. J. Thomson, "Silicon optical modulators," Nat. Photonics **4**(8), 518–526 (2010).
2. T. D. Bucio, A. Z. Khokhar, C. Lacava, S. Stankovic, G. Z. Mashanovich, P. Petropoulos, and F. Y. Gardes, "Material and optical properties of low-temperature NH3-free PECVD SiNxlayers for photonic applications," J. Phys. D: Appl. Phys. **50**(2), 025106 (2017).
3. K. Ikeda, R. E. Saperstein, N. Alic, and Y. Fainman, "Thermal and Kerr nonlinear properties of plasma-deposited silicon nitride/ silicon dioxide waveguides," Opt. Express **16**(17), 12987 (2008).
4. J. N. Milgram, J. Wojcik, P. Mascher, and A. P. Knights, "Optically pumped Si nanocrystal emitter integrated with low loss silicon nitride waveguides," Opt. Express **15**(22), 14679–14688 (2007).
5. R. Soref, "Tutorial: Integrated-photonic switching structures," APL Photonics **3**(2), 021101 (2018).
6. C. Ríos, M. Stegmaier, P. Hosseini, D. Wang, T. Scherer, C. D. Wright, H. Bhaskaran, and W. H. P. Pernice, "Integrated all-photonic non-volatile multi-level memory," Nat. Photonics **9**(11), 725–732 (2015).
7. J. Faneca, T. Perova, V. Tolmachev, and A. Baldycheva, "One-dimensional multi-channel photonic crystal resonators based on Silicon-On-Insulator with high quality factor," Front. Phys. **6**, 33 (2018).
8. F. Y. Gardes, G. T. Reed, N. Emerson, and C. Png, "A sub-micron depletion-type photonic modulator in silicon on insulator," Opt. Express **13**(22), 8845–8854 (2005).
9. D. J. Thomson, F. Y. Gardes, Y. Hu, G. Mashanovich, M. Fournier, P. Grosse, J.-M. Fedeli, and G. T. Reed, "High contrast 40gbit/s optical modulation in silicon," Opt. Express **19**(12), 11507–11516 (2011).
10. D. J. Thomson, F. Y. Gardes, J. Fedeli, S. Zlatanovic, Y. Hu, B. P. P. Kuo, E. Myslivets, N. Alic, S. Radic, G. Z. Mashanovich, and G. T. Reed, "50-gb/s silicon optical modulator," IEEE Photonics Technol. Lett. **24**(4), 234–236 (2012).
11. A. D. Neira, G. A. Wurtz, P. Ginzburg, and A. V. Zayats, "Ultrafast all-optical modulation with hyperbolic metamaterial integrated in si photonic circuitry," Opt. Express **22**(9), 10987–10994 (2014).
12. A. S. Shalin, P. Ginzburg, P. A. Belov, Y. S. Kivshar, and A. V. Zayats, "Nano-opto-mechanical effects in plasmonic waveguides," Laser Photonics Rev. **8**(1), 131–136 (2014).
13. S. Yu, X. Wu, Y. Wang, X. Guo, and L. Tong, "2d materials for optical modulation: Challenges and opportunities," Adv. Mater. **29**(14), 1606128 (2017).
14. M. Liu, X. Yin, and X. Zhang, "Double-layer graphene optical modulator," Nano Lett. **12**(3), 1482–1485 (2012).
15. H. Dalir, Y. Xia, Y. Wang, and X. Zhang, "Athermal broadband graphene optical modulator with 35 ghz speed," ACS Photonics **3**(9), 1564–1568 (2016).
16. Y. Ding, X. Zhu, S. Xiao, H. Hu, L. H. Frandsen, N. A. Mortensen, and K. Yvind, "Effective electro-optical modulation with high extinction ratio by a graphene–silicon microring resonator; PMID: 26042835.," Nano Lett. **15**(7), 4393–4400 (2015).
17. M. Mohsin, D. Neumaier, D. Schall, M. Otto, C. Matheisen, A. L. Giesecke, A. A. Sagade, and H. Kurz, "Experimental verification of electro-refractive phase modulation in graphene," Sci. Rep. **5**(1), 10967 (2015).
18. M. Romagnoli, V. Sorianello, M. Midrio, F. H. L. Koppens, C. Huyghebaert, D. Neumaier, P. Galli, W. Templ, A. D'Errico, and A. C. Ferrari, "Graphene-based integrated photonics for next-generation datacom and telecom," Nat. Rev. Mater. **3**(10), 392–414 (2018).
19. M. Romagnoli, "Graphene photonics for optical communications," *Optical Fiber Communication Conference (OFC) 2019* p. M3D.3 (2019).
20. K. S. Novoselov, V. I. Fal, L. Colombo, P. R. Gellert, M. G. Schwab, K. Kim, V. I. F. Ko, L. Colombo, P. R. Gellert, M. G. Schwab, and K. Kim, "A roadmap for graphene," Nature **490**(7419), 192–200 (2012).
21. A. B. Kuzmenko, E. Van Heumen, F. Carbone, and D. Van Der Marel, "Universal optical conductance of graphite," Phys. Rev. Lett. **100**(11), 117401 (2008).
22. R. R. Nair, P. Blake, A. N. Grigorenko, K. S. Novoselov, T. J. Booth, T. Stauber, N. M. R. Peres, and A. K. Geim, "Fine Structure Constant Defines Visual Transparency of Graphene," Science **320**(5881), 1308 (2008).
23. F. Wang, Y. Zhang, C. Tian, C. Girit, A. Zettl, M. Crommie, and Y. R. Shen, "Gate-Variable Optical Transitions in Graphene," Science **320**(5873), 206–209 (2008).
24. N. A. Hassan and R. Hijazi, "Chapter 6 - data hiding forensics," in *Data Hiding Techniques in Windows OS*, N. A. Hassan and R. Hijazi, eds., (Syngress, Boston, 2017), pp. 207–265.
25. J. Andréasson, U. Pischel, S. D. Straight, T. A. Moore, A. L. Moore, and D. Gust, "All-photonic multifunctional molecular logic device," J. Am. Chem. Soc. **133**(30), 11641–11648 (2011).
26. Y. Fu, X. Hu, C. Lu, S. Yue, H. Yang, and Q. Gong, "All-optical logic gates based on nanoscale plasmonic slot waveguides," Nano Lett. **12**(11), 5784–5790 (2012).
27. H. Li, Y. Anugrah, S. J. Koester, and M. Li, "Optical absorption in graphene integrated on silicon waveguides," Appl. Phys. Lett. **101**(11), 111110 (2012).
28. J. Lin, Q. Tong, Y. Lei, Z. Xin, D. Wei, X. Zhang, J. Liao, H. Wang, and C. Xie, "Electrically tunable infrared filter based on a cascaded liquid-crystal Fabry-Perot for spectral imaging detection," Appl. Opt. **56**(7), 1925 (2017).

Optics EXPRESS

29. T. D. Bucio, A. Z. Khokhar, G. Z. Mashanovich, and F. Y. Gardes, "N-rich silicon nitride angled MMI for coarse wavelength division (de)multiplexing in the O-band," Opt. Lett. **43**(6), 1251 (2018).
30. A. N. Obraztsov, "Making graphene on a large scale," Nat. Nanotechnol. **4**(4), 212–213 (2009).
31. X. Hu and J. Wang, "High Figure of Merit Graphene Modulator Based on Long-Range Hybrid Plasmonic Slot Waveguide," IEEE J. Quantum Electron. **53**(3), 1–8 (2017).
32. Y.-C. Chang, C.-H. Liu, Z. Zhong, and T. B. Norris, "Extracting the complex optical conductivity of true two-dimensional layers by ellipsometry," in *2014 Conference on Lasers and Electro-Optics (CLEO) - Laser Science to Photonic Applications*, (2014), pp. 1–2.
33. Q. Bao and K. P. Loh, "Graphene photonics, plasmonics, and broadband optoelectronic devices," ACS Nano **6**(5), 3677–3694 (2012).
34. A. J. Stapleton, C. J. Shearer, C. T. Gibson, A. D. Slattery, and J. G. Shapter, "Accurate thickness measurement of graphene," Nanotechnology **27**(12), 125704 (2016).
35. C. T. Phare, Y.-H. D. Lee, J. Cardenas, and M. Lipson, "Graphene electro-optic modulator with 30 ghz bandwidth," Nat. Photonics **9**(8), 511–514 (2015).
36. P. Gunter, "Electro-optical effects in ferroelectrics," Ferroelectrics **74**(1), 305–307 (1987).
37. W. Zhu, D. Neumayer, V. Perebeinos, and P. Avouris, "Silicon nitride gate dielectrics and band gap engineering in graphene layers," Nano Lett. **10**(9), 3572–3576 (2010).
38. K. Luke, Y. Okawachi, M. R. E. Lamont, A. L. Gaeta, and M. Lipson, "Broadband mid-infrared frequency comb generation in a Si_3N_4 microresonator," Opt. Lett. **40**(21), 4823 (2015).
39. C. H. Ng, K. W. Chew, and S. F. Chu, "Characterization and comparison of pecvd silicon nitride and silicon oxynitride dielectric for mim capacitors," IEEE Electron Device Lett. **24**(8), 506–508 (2003).
40. P. Dong, W. Qian, H. Liang, R. Shafiiha, N.-N. Feng, D. Feng, X. Zheng, A. V. Krishnamoorthy, and M. Asghari, "Low power and compact reconfigurable multiplexing devices based on silicon microring resonators," Opt. Express **18**(10), 9852–9858 (2010).
41. E. J. Klein, D. H. Geuzebroek, H. Kelderman, G. Sengo, N. Baker, and A. Driessen, "Reconfigurable optical add-drop multiplexer using microring resonators," IEEE Photonics Technol. Lett. **17**(11), 2358–2360 (2005).
42. E. J. Klein and A. Driessen, "Densely integrated photonic devices based on microring resonators in access networks," in *2007 9th International Conference on Transparent Optical Networks*, vol. 1 (2007), p. 201.
43. M. Midrio, S. Boscolo, M. Moresco, M. Romagnoli, C. D. Angelis, A. Locatelli, and A.-D. Capobianco, "Graphene–assisted critically–coupled optical ring modulator," Opt. Express **20**(21), 23144–23155 (2012).
44. J. K. S. Poon, J. Scheuer, S. Mookherjea, G. T. Paloczi, Y. Y. Huang, and A. Yariv, "Matrix analysis of microring coupled-resonator optical waveguides," Opt. Express **12**(1), 90–103 (2004).
45. G. Kovacevic, C. Phare, S. Y. Set, M. Lipson, and S. Yamashita, "Ultra-high-speed graphene optical modulator design based on tight field confinement in a slot waveguide," Appl. Phys. Express **11**(6), 065102 (2018).
46. A. Venugopal, L. Colombo, and E. M. Vogel, "Contact resistance in few and multilayer graphene devices," Appl. Phys. Lett. **96**(1), 013512 (2010).
47. W. S. Leong, X. Luo, Y. Li, K. H. Khoo, S. Y. Quek, and J. T. Thong, "Low resistance metal contacts to MoS 2 devices with nickel-etched-graphene electrodes," ACS Nano **9**(1), 869–877 (2015).
48. V. Sorianello, M. Midrio, and M. Romagnoli, "Design optimization of single and double layer Graphene phase modulators in SOI," Opt. Express **23**(5), 6478 (2015).
49. J. K. Lee, C. S. Park, and H. Kim, "Sheet resistance variation of graphene grown on annealed and mechanically polished Cu films," RSC Adv. **4**(107), 62453–62456 (2014).
50. R. Ishikawa, Y. Kurokawa, S. Miyajima, and M. Konagai, "Peeling process of thin-film solar cells using graphene layers," Appl. Phys. Express **10**(8), 082301 (2017).